aerospace

MDPI

Article

Numerical Investigation of Frequency Acceleration Effect on Aerodynamic Characteristics of 2-DoF Flapping Wing in Hovering

Fanwei Kong [1], Zhandong Li [2,*], Ligang Qu [2,*] and Jing Li [3]

[1] School of Aeronautics and Astronautics, Shenyang Aerospace University, Shenyang 110136, China; kongfanwei@chinacfi.net
[2] Civil Aviation School, Shenyang Aerospace University, Shenyang 110136, China
[3] Aviation Manufacturing Technology Digital Defense Key Discipline Laboratory, Shenyang Aerospace University, Shenyang 110136, China; 20133362@sau.edu.cn
* Correspondence: lizhandong365@163.com (Z.L.); quligang@126.com (L.Q.)

Abstract

This study employed numerical simulations to investigate the aerodynamic characteristics of a flapping wing by solving the governing incompressible Navier–Stokes equations. Using computational fluid dynamics (CFD), the effect of frequency acceleration on the aerodynamic performance of a two-degrees-of-freedom (DoF) flapping wing in hovering was examined. The results indicate that the pitching frequency acceleration significantly influences the aerodynamic force: positive acceleration enhances lift by up to 2.0 times while maintaining propulsion compared to the case under negative acceleration. This mechanism is attributed to the delayed shedding of the leading-edge vortex (LEV) and the shedding of the trailing-edge vortex (TEV). Moreover, aerodynamic forces are also affected by plunge acceleration, with both negative and positive acceleration contributing to performance improvement. An increase in the acceleration coefficient leads to a notable enhancement in the aerodynamic force; however, the improvement becomes marginal when the coefficient n exceeds 0.4. The underlying flow evolution is illustrated and analyzed through pressure and vorticity contours. These findings on the acceleration effect will be applied to optimize the kinematics and design of flapping wing drones.

Keywords: 2-DoF flapping wing; frequency acceleration; aerodynamic performance; numerical simulation

Check for updates

Academic Editor: Kung-Ming Chung

Received: 26 November 2025
Revised: 5 January 2026
Accepted: 6 January 2026
Published: 8 January 2026

Copyright: © 2026 by the authors. Licensee MDPI, Basel, Switzerland. This article is an open access article distributed under the terms and conditions of the Creative Commons Attribution (CC BY) license.

1. Introduction

In nature, the bird and insect species that rely on flapping wings possess exceptional flight capabilities—including forward flight, hovering, and even backward flight [1,2]. These flyers are able to maintain remarkable maneuverability in low Reynolds numbers (10^3~10^4), as evidenced by numerous biological studies [3–5]. Indeed, such a characteristic, particularly the unsteady aerodynamic behaviors involved [6,7], has attracted significant interests of researchers. Considerable efforts have therefore been devoted to uncovering the underlying mechanisms of flapping flight in order to thoroughly understand its fundamental nature.

To investigate the aerodynamic performance of flapping wings, three primary methodologies are commonly employed: quasi-steady modeling [8], experimental testing [9], and numerical simulation [10]. In practice, the flapping motion of birds and insects involves

significant unsteady effects due to its high frequency, rendering quasi-steady models inadequate for accurately determining aerodynamic forces, which can often lead to erroneous results [11–13]. Alternatively, wind tunnel experiments [14–16] offer a more precise approach for studying flapping wing aerodynamics, allowing detailed flow field analysis through techniques such as particle image velocimetry (PIV). However, the widespread adoption of such experimental methods is often constrained by their long development cycles and high costs.

In recent decades, numerical simulations have become an increasingly common method for determining the aerodynamic forces of flapping wings. This approach has been extensively employed and yielded numerous findings. Research interest in numerical methods was initially sparked by the influence of flight conditions—such as the Reynolds number and advance ratio [17–19], as well as geometrical parameters, including aspect ratio, corrugation [20–22], and wing arrangements [23,24]—on aerodynamic performance and flow field characteristics. Furthermore, the influence of motion modes on aerodynamic performance is also considered. Li et al. [25] performed a numerical simulation to investigate how flapping frequency, amplitude, and the chordal torsion angle affected aerodynamic performance. Their results demonstrated that increasing the frequency significantly enhanced instantaneous lift, whereas increasing the amplitude yielded only a minor improvement. In another study, Wu et al. [26] incorporated a surging motion into an airfoil undergoing combined pitching and plunging, and examined the effect of the phase angle between surging and plunging on the aerodynamic performance. Their numerical simulations demonstrated that optimal aerodynamic performance was achieved when the phase angle ranged between 15° and 90°. Mekadem et al. [27] examined the influence of wingtip trajectory—specifically, the combination of sinusoidal plunging with pitching motion—on the propulsive performance of a flapping wing. Their results showed that the highest propulsive efficiency was achieved under a sinusoidal trajectory, while also underscoring the significant role of plunge frequency in lift generation. Using an overset mesh approach, Lang et al. [28] systematically investigated the aerodynamic efficiency of an owl-like airfoil undergoing bio-inspired flapping kinematics. They found that the airfoil exhibited a noticeable increase in lift, outperforming its counterpart following a pure sinusoidal motion. By employing a modified elliptic function to generate different wingtip trajectories, Boudis et al. [29] numerically investigated the effect of non-sinusoidal motion on propulsion. Their findings revealed that non-sinusoidal flapping considerably influenced propulsion, with the optimal performance attained under sinusoidal motion. The numerical study by Wang et al. [30] on hovering flapping wings revealed that aerodynamic force was reduced by the deviation from the stroke plane, while an increased angle of attack elevated drag and power consumption.

The flapping motion of insects is highly intricate, and insufficient attention has been given to the wingtip trajectory and associated motion parameters. In particular, the asymmetry in flapping kinematics—where the frequency and the duration of the downstroke and upstroke are significantly different—cannot be overlooked. Sarkar et al. [31] used a numerical model to study the aerodynamic performance of a dragonfly's flapping wing in hovering. Their results demonstrated that a reduction in the downstroke duration enhanced both lift and propulsion. Similar observations were reported in other studies [32], where the instantaneous vortical structure helped to clarify the mechanism responsible for fluctuations in lift. Hu et al. [33] investigated the effect of asymmetric deviation motion on the aerodynamic performance of flapping wings. Their results demonstrated that this asymmetry induced significant fluctuations in the instantaneous force. Furthermore, the lift was substantially enhanced as the deviation amplitude increased. While the role of asymmetrical flapping, particularly plunge asymmetry, in governing aerodynamic charac-

teristics has been established, a comprehensive understanding of its effects on other single degrees of freedom and a combination of acceleration of multiple degrees of freedom is still lacking. Moreover, the mechanism responsible for the observed variations in aerodynamic performance has not yet been fully elucidated. Furthermore, an asymmetry arises from the varying frequencies between different strokes. Consequently, frequency is prioritized over duration as a key parameter. The duration asymmetry between the downstroke and upstroke can be expressed in terms of frequency acceleration, defined as the ratio of the downstroke frequency to that of the upstroke. The effect of the frequency acceleration on aerodynamic performance in hovering [34,35] is investigated using CFD. The performance is quantified for cases with no acceleration, as well as with frequency acceleration in plunge, pitching, and combined pitching–plunge motions.

This study systematically investigates the influence of frequency acceleration on the aerodynamic performance of a 2-DoF flapping wing in hovering. In Section 2, the geometric model of the flapping wing is presented, along with kinematic equations in hovering accounting for the frequency acceleration effect. Section 3 describes the numerical methodology employed to analyze the aerodynamic behavior of a flapping wing in hovering. The resulting aerodynamic forces are reported in Section 4, and flow field snapshots are examined to elucidate underlying physical mechanisms. Finally, several key conclusions are drawn.

2. Model and Kinematics

2.1. Kinematic Model

In this section, a classical airfoil NACA0012 is employed to simulate the flapping wing motion of insects. Generally, motion equations of 2-DoF flapping wings, which include both plunge and pitching motions, are expressed as follows:

$$h(t) = h_0 + h_m \cos(2\pi f t) \tag{1}$$

$$\theta(t) = \theta_0 + \theta_m \cos(2\pi f t + \varphi) \tag{2}$$

where h_0 and θ_0 are, respectively, the initial value of plunge and pitching motion, h_m and θ_m are the plunge and pitching amplitude, ϕ is the phase angle between plunge and pitching, and f is the flapping frequency.

It is observed that the duration of the downstroke is notably shorter than that of the upstroke [36]. The frequency acceleration effect (FAE) is defined as the ratio of flapping frequency during the downstroke (f_d) to that during the upstroke (f_u). To quantify this variation, a frequency acceleration coefficient, denoted as k_i, is expressed as follows:

$$k_i = \frac{f_{id}}{f_{iu}} \tag{3}$$

where the subscript i signifies the type of coefficient, with k_h and k_θ being the frequency acceleration coefficients pertaining to the plunge and pitching motion, respectively.

To clarify the frequency variation under the FAE, a flapping cycle is divided into two phases. Using the plunge motion at an inclined angle α as an example, the schematic of the 2-DoF flapping wing is shown in Figure 1. Phase A (from A_1 to A_3) corresponds to the downstroke with an acceleration frequency of $k_h f$, while Phase B (from B_3 to B_1) represents the upstroke with a constant frequency f. These two phases repeat continuously in each subsequent cycle.

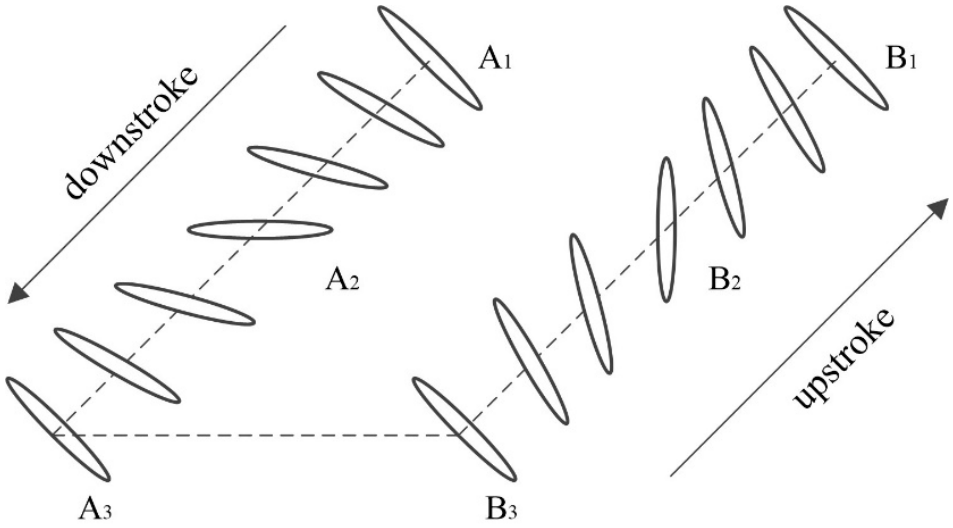

Figure 1. The schematics of 2-DoF flapping wing under FAE.

Given the conditions of the FAE, the frequency in the downstroke is no longer equivalent to that in the upstroke. As a result, Equation (1) is transformed as follows:

$$h(t) = h_0 + h_m \cos[2\pi k_h f(t-(n-1)\cdot t_{hA})](n-1)T_{h*} \le t < \frac{1}{2k_h f} + (n-1)T_{h*} \quad (4a)$$

$$h(t) = h_0 + h_m \cos[2\pi f(t+n\cdot t_{hB})]\frac{1}{2k_h f} + (n-1)T_{h*} \le t < n\cdot T_{h*} \quad (4b)$$

where n is the number of plunge cycles. The deviation time of acceleration is t_{hA}, which is $\frac{k_h-1}{2k_h f}$; the deviation time of deceleration is t_{hB}, which is $\frac{k_h-1}{2k_h f}$. T_{h^*} is the variable frequency cycle in the plunge motion, which is $\frac{k_h+1}{2k_h f}$.

In the following, the phase angle ϕ is set as $-\pi/2$, so that the initial pitching angle is centered. A complete pitching cycle is divided into three phases: the first phase ($A_1 \to A_2$) corresponds to half of the downstroke with an initial frequency f; the second phase ($A_2 \to A_3 \to B_3 \to B_2$) involves an accelerated pitching motion with a frequency increased by $k_\theta f$; and the third phase ($B_2 \to B_1 \to A_1 \to A_2$) restores the pitching frequency to the initial value f. The second and third phases are continuously repeated. Accordingly, Equation (2) is rewritten as follows:

$$\theta(t) = \theta_0 + \theta_m \sin(2\pi f t) 0 < t \le \frac{1}{4f} \quad (5a)$$

$$\theta(t) = \theta_0 + \theta_m \sin\{2\pi k_\theta f[t-(2n-1)\cdot t_{\theta A}]\}\frac{1}{4f} + (n-1)T_{\theta*} < t \le \frac{k_\theta+2}{4k_\theta f} + (n-1)T_{\theta*} \quad (5b)$$

$$\theta(t) = \theta_0 + \theta_m \sin[2\pi f(t+2n\cdot t_{\theta B})]\frac{k_\theta+2}{4k_\theta f} + (n-1)T_{\theta*} < t \le \frac{k_\theta+1}{2k_\theta f} + (n-1)T_{\theta*} \quad (5c)$$

where the deviation time of acceleration is $t_{\theta A}$ and $t_{\theta B}$, which is $\frac{k_\theta-1}{4k_\theta f}$; T_{θ^*} is the variable frequency cycle, which is $\frac{k_\theta+1}{2k_\theta f}$.

2.2. Kinematics Under FAE

Under the influence of the FAE, the flapping cycle of a 2-DoF flapping wing is altered, a behavior closely linked to the FAE coefficient k_i. As a result, the flapping trajectory can no longer be accurately described by a simple harmonic function. In this subsection, taking the plunge motion as an example, Equations (4a) and (4b) are fitted into a functional form

following the methodology processed in reference [37]. For a plunge acceleration of k_h = 1.2 and amplitude of h_m = 1.4 c (where c = 0.01 m), the fitted expression for the plunge velocity is given as follows:

$$\begin{aligned}\dot{h}(t) = \; & 0.001859 - 1.969\cos(2\pi ft) - 13.55\sin(2\pi ft) + \\ & 1.352\cos(4\pi ft) - 0.3966\sin(4\pi ft) + \\ & 0.07535\cos(6\pi ft) + 0.1658\sin(6\pi ft)\end{aligned} \tag{6}$$

By analogy, corrected functions of plunge velocity and displacement are derived for the coefficient k_h ranging from 1.0 to 1.5 with an increment of 0.1. With an initial frequency of f = 10 Hz, the temporal variations in velocity and displacement during a cycle without acceleration are illustrated in Figure 2. Among them, V_h (m/s) is the velocity of plunge and h (m) is the plunge displacement.

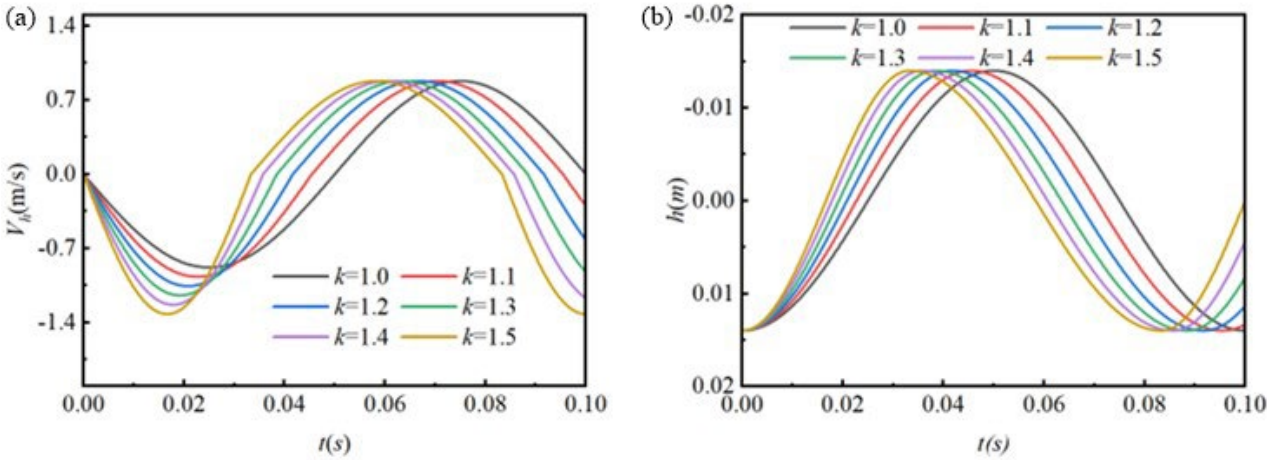

Figure 2. The velocity and displacement of a cycle in the plunge. The motion curve of a cycle in the plunge: (**a**) the plunge velocity Vh; (**b**) the plunge displacement h.

As indicated in Figure 2, the flapping cycle duration is markedly reduced when the frequency effect is considered, compared to the non-accelerated case. To account for acceleration effects in frequency measurements, the average flapping frequency $\overline{f}_i$ is defined as follows:

$$\frac{1}{\overline{f}_i} = \frac{1}{2f_{iu}} + \frac{1}{2f_{id}} \tag{7}$$

As indicated by Equation (7), the relationship between the cycle with and without the frequency acceleration is given as follows:

$$T_i = \frac{2k_i}{1+k_i}\overline{T}_i \tag{8}$$

where $\overline{T}_i$ is the cycle with frequency acceleration, and is used for a short cycle of a flapping wing, and T_i is the cycle without frequency acceleration.

The average aerodynamic force is a key metric for evaluating aerodynamic performance, typically derived from the average value of the force coefficient over a short cycle. However, due to frequency acceleration, such a short interval no longer corresponds to a complete flapping cycle—that is, the airfoil does not return to its initial position and posture within this time. Therefore, in the following section, the analysis postulates a long cycle, in which the airfoil returns to its starting point after a duration encompassing an integral number of short cycles. The resulting aerodynamic force is determined by taking its average over this complete long cycle.

3. Numerical Method

An investigation into the influence of frequency acceleration on the aerodynamic characteristics of a 2-DoF flapping wing is conducted by CFD. The present section describes the numerical simulation framework, encompassing the solver setup, the validation of this method, and analysis of both grid and time-step independence.

3.1. Solver Setting

This subsection investigates the aerodynamic performance and flow field characteristics of a 2-DoF flapping wing under the FAE through numerical simulations. A computational approach based on ANSYS Fluent is employed to solve the incompressible Navier–Stokes equations that govern the flow dynamics.

To account for the unsteady effects induced by flapping wings, the overset mesh technique is employed in ANSYS Fluent 2022, which consists of background mesh and component mesh. This approach helps to avoid the generation of negative mesh volume and is well-suited for large-amplitude flapping motions. The background mesh remains stationary throughout the simulation, while the component mesh moves as a rigid body, fully governed by a User-Defined Function (UDF), according to Equations (4) and (5).

As shown in Figure 3, the computational domain is divided into component and background zones, making it suitable for overset mesh technology. The background zone measures 30 c × 20 c (length × width), while the component zone is circular with a radius of r = 3 c. An airfoil is positioned at the center of the component zone. A fixed coordinate system, O-xy, is established with its origin at the center of the airfoil, which also serves as the pivot of pitching motion.

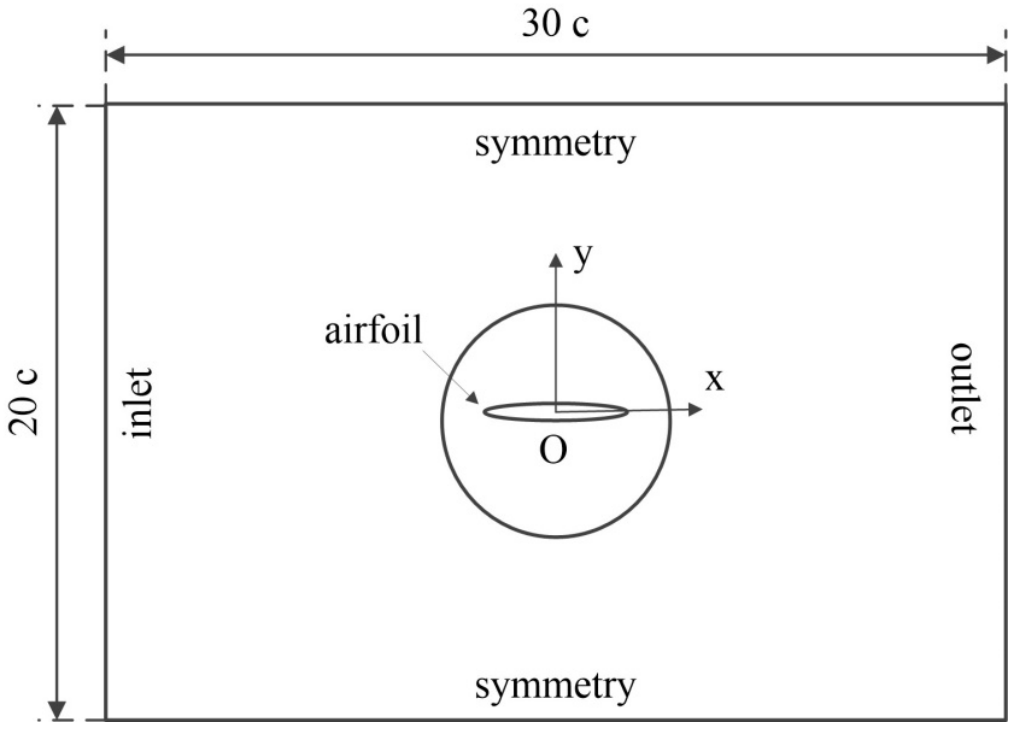

Figure 3. The computational domain of 2-DoF flapping wing.

In the computational domain, the left and right boundaries are specified as a velocity inlet and a pressure outlet, respectively. The stream velocity in the inlet is set to zero in hovering, while the pressure outlet is maintained at the atmospheric pressure. The upper and lower boundaries are treated as symmetrical planes. The component boundary is defined as an overset, and the remaining boundaries are modeled as no-slip walls.

Figure 4 illustrates the mesh of the computational domain employed in the simulation. In the component zone, the first layer's thickness is set as 0.0005c, achieving $y^+ \approx 1$, with subsequent layers progressively expanding from the airfoil surface toward the overset boundary. In contrast, the background zone maintains a uniform mesh size, comparable to that used in the component region. The overall assembled mesh, the component mesh, and a detailed local view are presented in Figure 4a, Figure 4b, and Figure 4c, respectively.

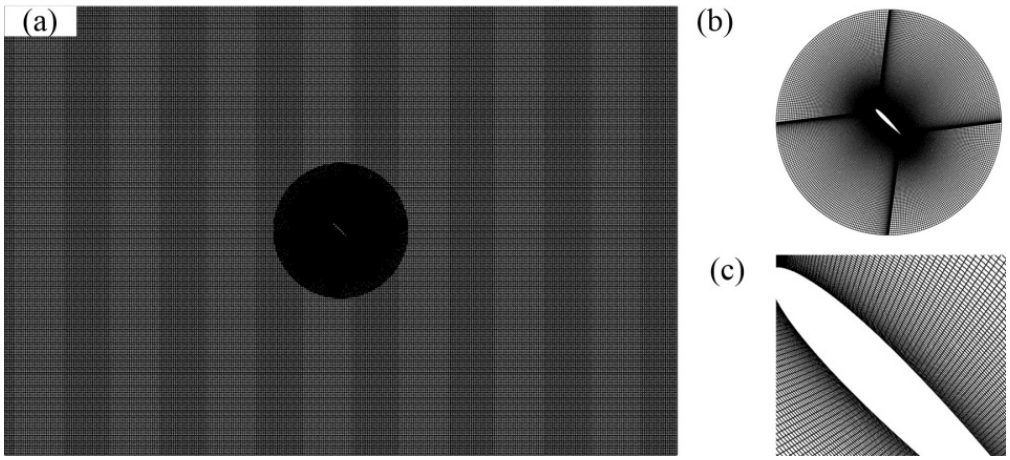

Figure 4. The mesh of the computational domain: (**a**) the assembled mesh; (**b**) the component mesh; (**c**) the boundary layer mesh.

The Reynolds number, *Re*, is represented as follows:

$$\mathrm{Re} = \frac{\rho U_{ref} c}{\mu} \tag{9}$$

where μ (=1.87 × 10^{-5} Pa·s) is the dynamic viscosity coefficient of air, ρ (=1.225 kg/m^3) is the air density, c (=0.01 m) is the chord length, and U_{ref} (=$2\pi h_m f$,) is the maximum velocity of the wingtip.

As indicated by Equation (9), the Reynolds number (*Re*) reaches 5.7 × 10^2 at a frequency of 10 Hz. Consequently, the laminar flow model is adopted in this work to simulate the flow field. The parameters of numerical simulation are set as follows: a second-order accurate interpolation scheme is employed, with four interpolation buffer layers. The flow courant number is set as 200. The coupled algorithm is employed for pressure–velocity coupling. The spatial discretization of the gradient, pressure, and momentum is, respectively, least squares cell-based, second-order, and second-order upwind. The explicit relaxation factors of momentum and pressure are 0.75, and the under-relaxation factors of density and body force are 1.0. The convergence criterion is that the residual value is less than 10^{-6}.

3.2. Method Verification

The preconditioned laminar Navier–Stokes equations are solved based on the Finite Volume Method (FVM). To validate the numerical approach presented in Section 3.1, computational results are compared with the experimental and numerical data from reference [38]. The study focuses on the NACA0012 airfoil, with the kinematic parameters set as follows: initial conditions, $h_0 = \theta_0 = 0°$; amplitudes, h_m = 0.025 m and $\theta_m = \pi/4$; the cycle T = 0.025 s; and the inclined angle $\alpha = \pi/3$. The average aerodynamic forces are computed by CFD at phase angles of $\phi = -\pi/4$, 0, and $\pi/4$. A comparison with the reference data [38] is presented in Figure 5.

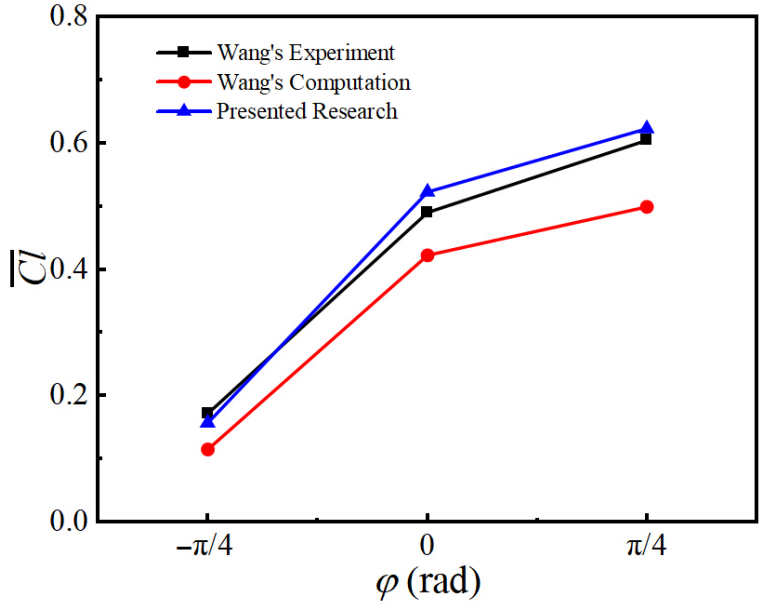

Figure 5. The comparison of the average aerodynamic force between the experiment and numerical simulation.

The values of the average lift and the errors between the simulation and experiment are shown in Table 1.

Table 1. The comparisons of the average lift between the simulation and experiment.

	$\varphi = -\pi/4$		$\varphi = 0$		$\varphi = \pi/4$	
	Cl	ε	Cl	ε	Cl	ε
Wang's Experiment	0.1721	-	0.4899	-	0.6041	-
Wang's Computation	0.1154	−32.95%	0.4223	−13.80%	0.499	−17.40%
Presented Research	0.1576	−8.42%	0.5224	6.63%	0.6225	2.95%

The instantaneous lift behavior is determined using the numerical method described in Section 3.1. The results are then compared against the experimental and computational data from reference [38], as shown in Figure 6.

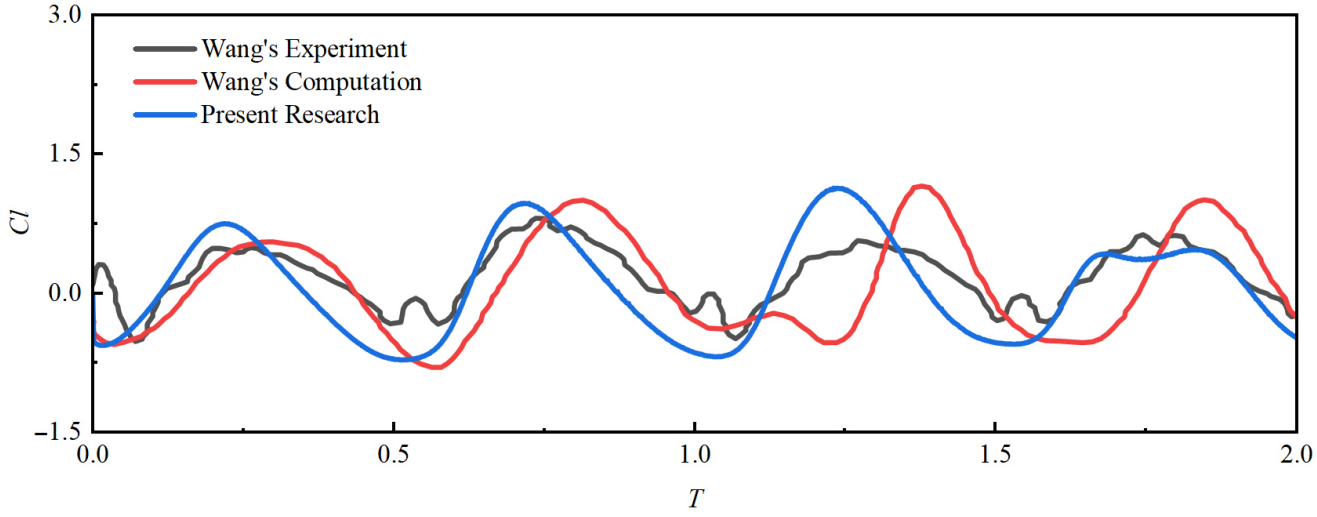

Figure 6. The comparison of lift coefficients between experiment and numerical simulation.

Figure 6 reveals a favorable agreement between the experimental and simulated aerodynamic coefficients at $\phi = 0°$, with a deviation within an allowable range. This level of agreement is deemed acceptable and demonstrates that the numerical method in Section 3.1 is both valid and reliable.

3.3. Resolution of Mesh and Time-Step

In this subsection, mesh and time-step resolution studies are conducted to ensure that numerical errors remain with an acceptable range. The mesh is refined uniformly, with cells clustered near the flapping wing surface. By adjusting the spacing increment ratio, three distinct meshes are generated: coarse, medium, and fine, as summarized in Table 2. With solver settings consistent with those described in Section 3.2, the resulting average aerodynamic forces and the corresponding errors (ε) are presented in Table 2.

Table 2. The average aerodynamic force and error under different types of meshes.

	Number of Grids	Cl_{mean}	ε_{Clmean}	Cl_{max}	ε_{Clmax}	Cd_{mean}	ε_{Cdmean}	Cd_{max}	ε_{Cdmax}
Coarse case	1.47×10^5	0.543	10.97%	2.732	3.96%	−0.557	−6.18%	−2.80	24.9%
Medium case	2.17×10^5	0.494	0.86%	2.638	0.38%	−0.594	−0.03%	−3.68	1.34%
Fine case	2.89×10^5	0.489	-	2.628	-	−0.594	-	−3.73	-

Similarly, instantaneous lift and drag coefficients are computed using the previously described numerical method for various mesh sizes, and the results are presented in Figure 7. Only a minor deviation is observed in the medium mesh case compared to the fine mesh case, indicating that mesh independence has been achieved between the two. Based on this outcome, the medium mesh is selected for all subsequent simulations.

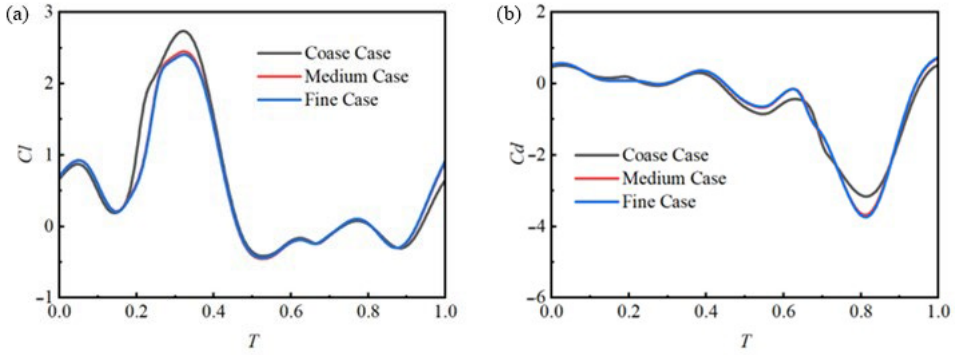

Figure 7. Instantaneous aerodynamic coefficients under different mesh resolutions: (**a**) lift; (**b**) drag.

A time-step resolution study is undertaken based on the medium case for a typical airfoil of NACA0012. Numerical simulations are executed using three types of temporal discretization: 250, 500, and 750 time-steps per flapping cycle. Table 3 presents the computed average aerodynamic forces and their respective errors.

Table 3. The average aerodynamic force and error under different time-steps.

	Cl_{mean}	ε_{Clmean}	Cl_{max}	ε_{Clmax}	Cd_{mean}	ε_{Cdmean}	Cd_{max}	ε_{Cdmax}
T/250	0.5203	5.77%	2.435	9.93%	−0.6376	6.35%	−3.502	9.61%
T/500	0.4935	8.16%	2.418	9.16%	−0.5939	1.69%	−3.617	13.21%
T/750	0.4592	-	2.215	-	−0.5877	-	−3.195	-

Instantaneous lift and drag coefficients are obtained using the numerical method described previously. The results for different time-step sizes are compared in Figure 8.

Minor variations in force coefficients are observed across the cases with different time-steps. The case with 500 time-steps per flapping cycle achieves a sufficiently accurate resolution. Therefore, this configuration is adopted in all subsequent simulations.

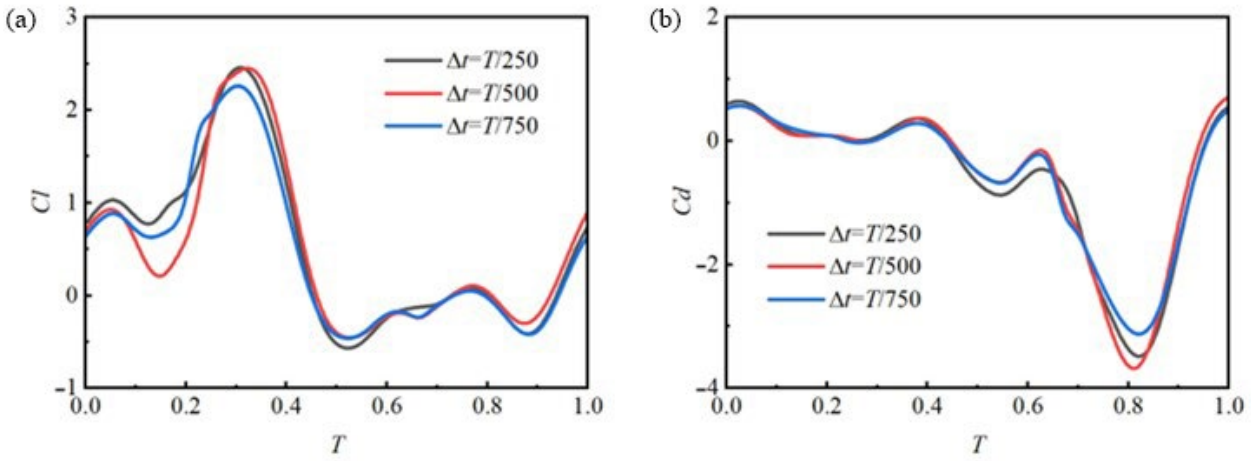

Figure 8. Instantaneous aerodynamic coefficients under different time-steps: (**a**) lift; (**b**) drag.

4. Results and Discussion

A key aspect of this investigation is the effect of frequency acceleration on aerodynamic performance. In the following analysis, the frequency acceleration mode and the acceleration coefficient are treated as variables influencing aerodynamic forces. The primary metrics for evaluating the aerodynamic performance of a 2-DoF flapping wing are aerodynamic coefficients—specifically, the lift coefficient C_l and the propulsion coefficient C_t—which are defined as follows:

$$C_l = \frac{F_L}{1/2\rho U_{ref}^2 c} \tag{10a}$$

$$C_t = \frac{-F_d}{1/2\rho U_{ref}^2 c} \tag{10b}$$

where F_L and F_d are, respectively, the lift and drag of a flapping wing.

The average lift coefficient $\overline{C}_l$, and the average propulsion coefficient $\overline{C}_t$, are defined as follows:

$$\overline{C}_l = \frac{1}{T}\int_0^T C_l dt \tag{11a}$$

$$\overline{C}_t = \frac{1}{T}\int_0^T C_t dt \tag{11b}$$

In the subsequent analysis, the parameters in Equations (1) and (2) are defined as follows: the plunge amplitude (h_m) and pitching amplitude (θ_m) of the flapping wing are set to $\pi/3$ and $\pi/12$, respectively; the initial positions h_0 and θ_0 are both zero; the phase angle $\phi = -\pi/2$; and the initial frequency ranges from 10 to 30 Hz, with a step size of 10 Hz.

4.1. Influence of Acceleration Mode on Aerodynamic Performance

This subsection examines how the acceleration mode—specifically, the combined effect of plunge and pitch acceleration—affects the aerodynamic performance of a 2-DoF flapping wing, as evaluated by CFD. In the subsequent analysis, the plunge acceleration during the upstroke is denoted as $+k_h$, while that during the downstroke is designated as $-k_h$. Similarly, k_θ and $-k_\theta$ represent the pitching acceleration in the anticlockwise and clockwise directions, respectively. The acceleration coefficients are set at k_i = 1.2, with

an initial frequency of f = 20 Hz. Various combinations of the acceleration coefficients are summarized in Table 4, encompassing cases of simultaneous plunge and pitching acceleration, in addition to isolated plunge acceleration.

Table 4. The coefficient combinations of frequency acceleration.

	k_h	k_θ		k_h	k_θ
AM-1	−1.2	1.0	AM-2	−1.2	−1.2
AM-3	−1.2	1.2	AM-4	1.2	1.0
AM-5	1.2	−1.2	AM-6	1.2	1.2
AM-7	1.0	1.0	AM-8	1.0	−1.2
AM-9	1.0	1.2			

As outlined in the numerical methodology of Section 3.1, CFD is employed to analyze the aerodynamic characteristics of a 2-DoF flapping wing in hovering. Therefore, the average aerodynamic forces under different acceleration modes are illustrated in Figure 9.

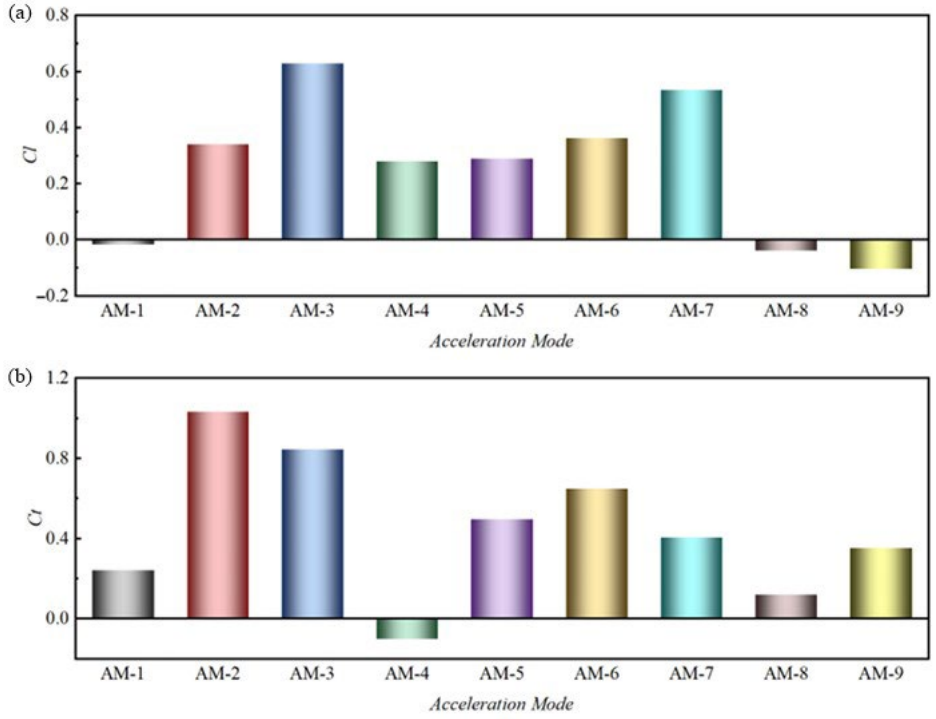

Figure 9. Average aerodynamic coefficients with different effect modes: (**a**) lift coefficient; (**b**) propulsion coefficient.

As shown in Figure 9, the aerodynamic lift of AM-3 is significantly greater than that of AM-7, which exhibits no acceleration. In contrast, the lift in other cases is only marginally lower than that of AM-7, and in some instances, it even becomes negative. While acceleration has the potential to enhance aerodynamic propulsion, plunge acceleration can substantially reduce it. Applying frequency acceleration to a single degree of freedom tends to degrade aerodynamic performance. On the other hand, simultaneously applying acceleration to both plunge and pitching motions is more effective in improving aerodynamic forces. In other words, AM-3 demonstrates superior aerodynamic performance across all scenarios.

Figure 10 illustrates the instantaneous variations in lift and propulsion coefficients for AM-1, AM-2, and AM-3 over a long cycle. This study aims to investigate the effect of pitching acceleration on the aerodynamic performance of a flapping wing.

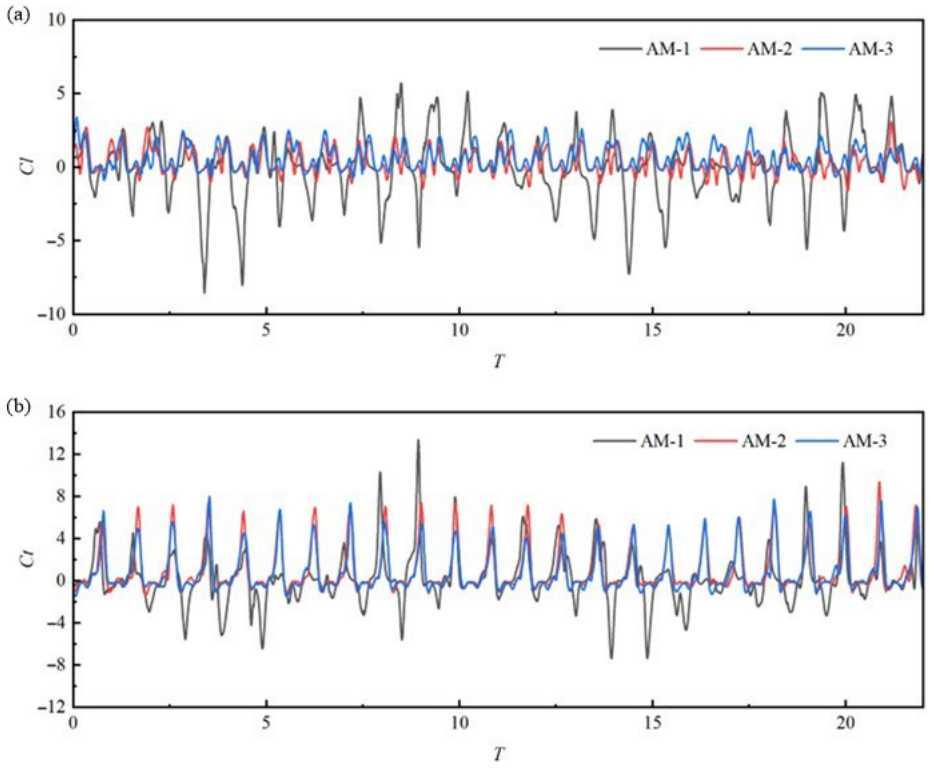

Figure 10. The time history of aerodynamic coefficients of AM-1, AM-2, and AM-3 in a long period: (**a**) lift coefficient; (**b**) propulsion coefficient.

As shown in Figure 10, lift fluctuations in the AM-1 case are more pronounced than in the other cases. Moreover, the minimum lift is lower, which leads to AM-1 exhibiting the lowest overall lift among all cases. In terms of propulsion, the variation pattern is similar to that of the instantaneous lift; however, the peak propulsion for AM-1 is higher than the maximum negative, resulting in positive average propulsion throughout the entire process. It is clearly demonstrated that the aerodynamic performance of AM-2 and AM-3 is significantly better than that of AM-1.

Figure 11 depicts the temporal variations in the aerodynamic forces of AM-1, AM-2, and AM-3 over a short cycle (the 22nd within the long-term cycle) to further investigate the pitching acceleration effect.

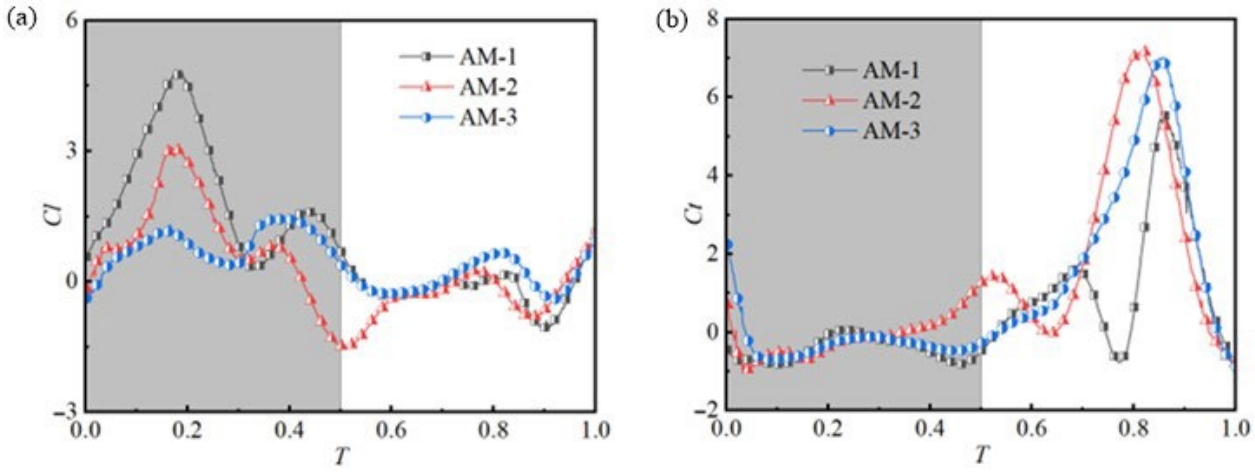

Figure 11. The time history of aerodynamic coefficients of AM-1, AM-2, and AM-3 in a short period: (**a**) lift coefficient; (**b**) propulsion coefficient.

In Figure 11 AM-1 exhibits the most significant variation in lift among the three cases, along with the highest recorded peak value. In addition, the trends in aerodynamic propulsion are remarkably consistent across the cases, with AM-2 and AM-3 reaching nearly identical peak values that substantially exceed that of AM-1. Moreover, both AM-2 and AM-3 clearly demonstrate superior average propulsion performance compared to AM-1.

To elucidate the short-term variation in the instantaneous aerodynamic force, Figure 12a–d present the pressure contours of AM-1, AM-2, and AM-3.

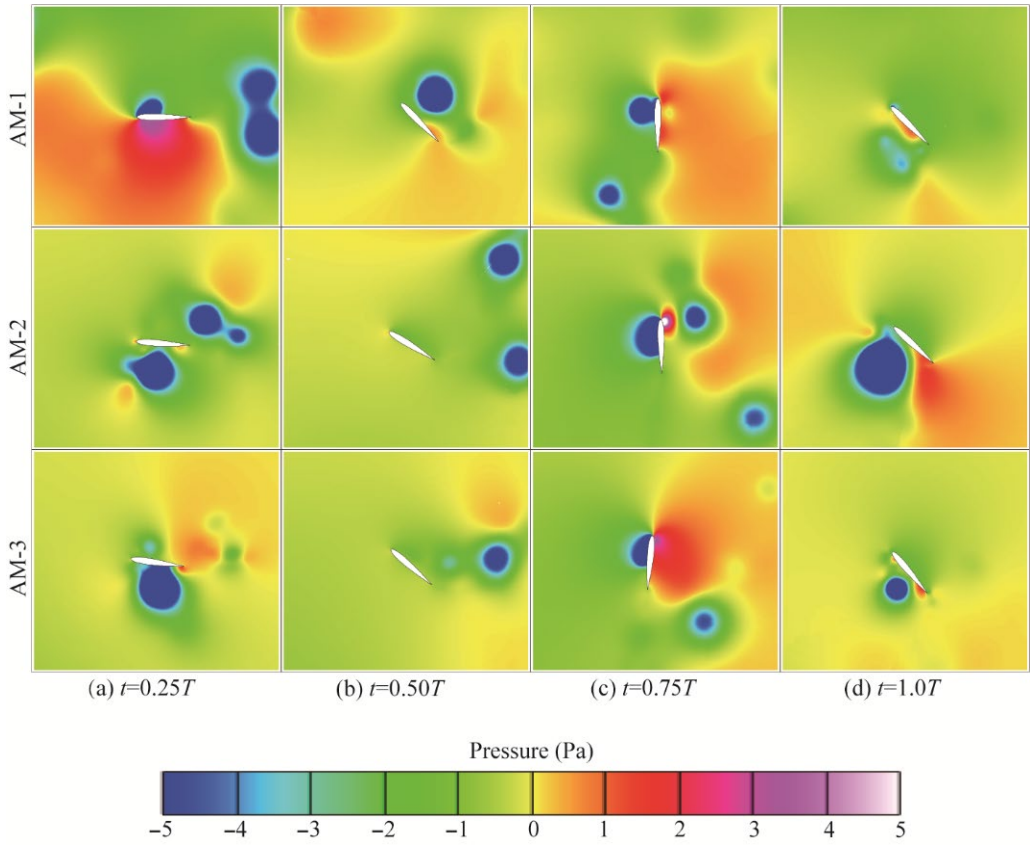

Figure 12. The pressure contours of AM-1, AM-2, and AM-3: (**a**) t = 0.25 T; (**b**) t = 0.50 T; (**c**) t = 0.75 T; (**d**) t = 1.0 T.

Figure 12a shows that the pressure on the lower surface for AM-1 is substantially higher than in the other cases, which results in positive lift at t = 0.25 T. In Figure 12b, the suction levels on the lower and upper surfaces are nearly identical across all cases, suggesting that lift is diminished and approaches zero by t = 0.5 T. As shown in Figure 12c, with a pitching displacement of $\pi/2$ at the end of the upstroke, the propulsion is generated by the pressure difference between the upper and lower surfaces. Here, the pressures of AM-2 and AM-3 are markedly greater than that of AM-1 at t = 0.75 T. In Figure 12d, the suction on the upper surface is almost equal to that on the lower surface, leading to a reduction in both lift and propulsion to nearly zero.

To closely investigate variations in aerodynamic forces, it is essential to examine the flow field near the airfoil. The vortical structures of AM-1, AM-2, and AM-3 are depicted in Figure 13a–d. In the following analysis, vorticity is adopted as an appropriate criterion for visualizing the vortical structures around the flapping wing. A clockwise vortex corresponds to negative vorticity, whereas an anticlockwise vortex is associated with positive vorticity.

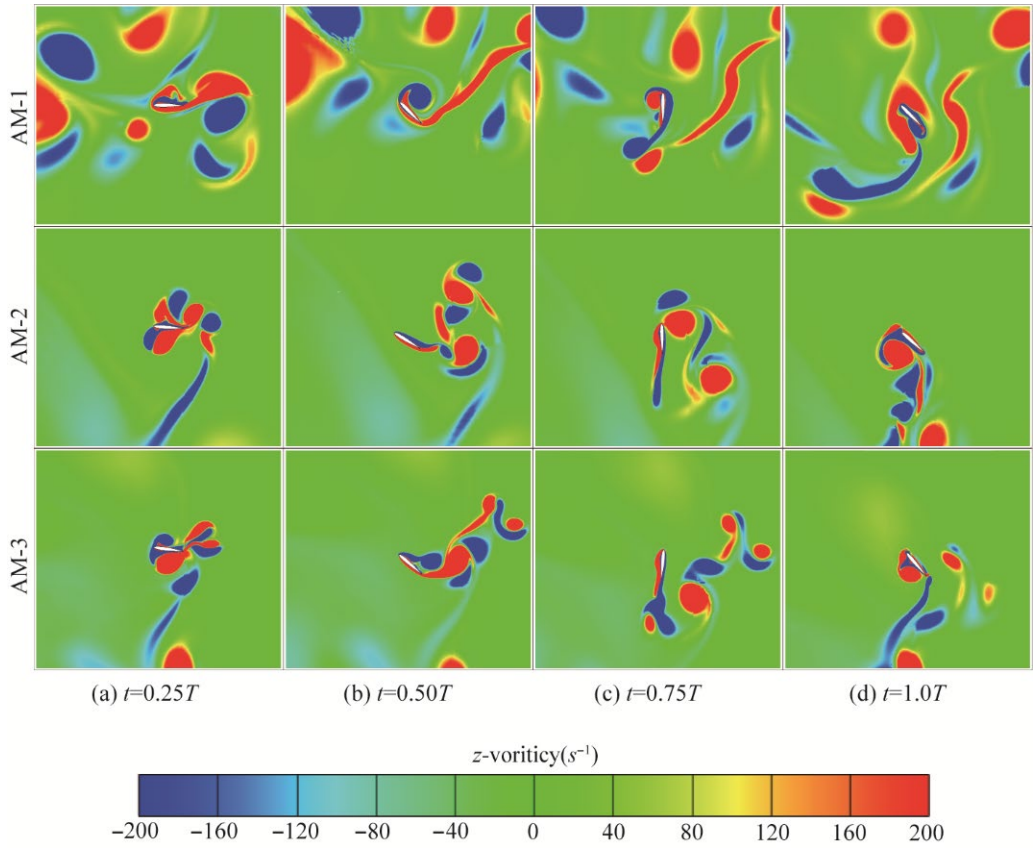

Figure 13. The vorticity contour of AM-1, AM-2, and AM-3: (**a**) t = 0.25 T; (**b**) t = 0.50 T; (**c**) t = 0.75 T; (**d**) t = 1.0 T.

Figure 13a shows that in all cases, anticlockwise LEVs are formed as a result of vortex shedding. Notably, both the strength and size of the LEVs in the AM-1 mode are significantly greater than those in the other cases. The anticlockwise LEVs enlarge the lift by enhancing the suction on the upper surface, suggesting that the AM-1 mode produces the highest instantaneous lift at t = 0.25 T, corresponding to the delayed stall. In Figure 13b, vortices are shed from the surface during the stall, leading to a reduction in suction and pressure. The lift is sharply decreased due to the airfoil in the stall. For the AM-1 and AM-3 modes, the intensity of LEV shedding near the surface is considerably weaker compared to the AM-2 mode. As a result, the instantaneous lift of AM-1 and AM-3 is nearly identical and higher than that of AM-2, which aligns with earlier observations at t = 0.5 T. Figure 13c depicts the shedding of TEVs in all cases, and the formation of anti-Kármán Vortex Street can sustain continuous propulsion, illustrating the flow behavior at t = 0.75 T. Finally, Figure 13d demonstrates that the strength of the shed TEVs is reduced across all cases, indicating a corresponding decrease in propulsion.

Figure 14 presents the temporal evolution of the aerodynamic coefficients for AM-3, AM-6, and AM-9 over a long cycle. This facilitates an analysis of how frequency acceleration in the plunge direction influences the aerodynamic performance of a 2-DoF flapping wing.

As shown in Figure 14, the minimum lift of AM-9 is significantly lower than that of the other cases. Moreover, the magnitude of this negative lift exceeds its maximum positive lift, leading to a negative average lift. In terms of propulsion, AM-3 exhibits the highest peak among the three cases, while its minimum value is the lowest. Consequently, the average propulsion of AM-3 surpasses that of the others, which is consistent with the previous findings.

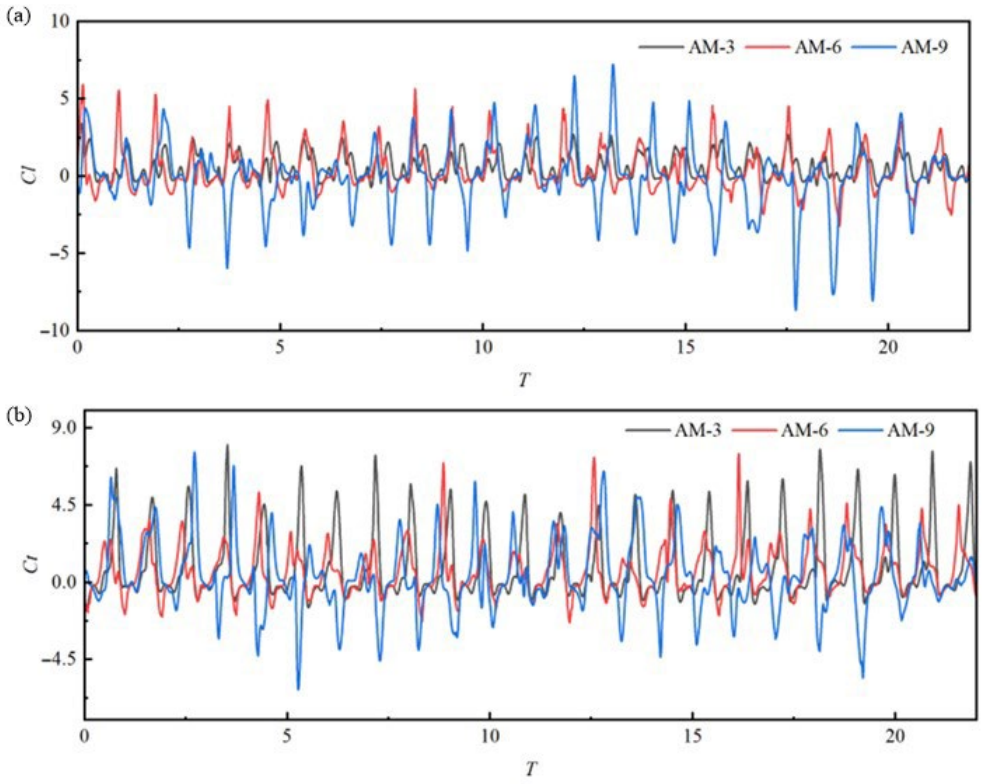

Figure 14. The time history of aerodynamic coefficients of AM-3, AM-6, and AM-9 in a long period: (**a**) lift coefficient; (**b**) propulsion coefficient.

The instantaneous aerodynamic performances of AM-3, AM-6, and AM-9 in a short cycle are shown in Figure 15a,b.

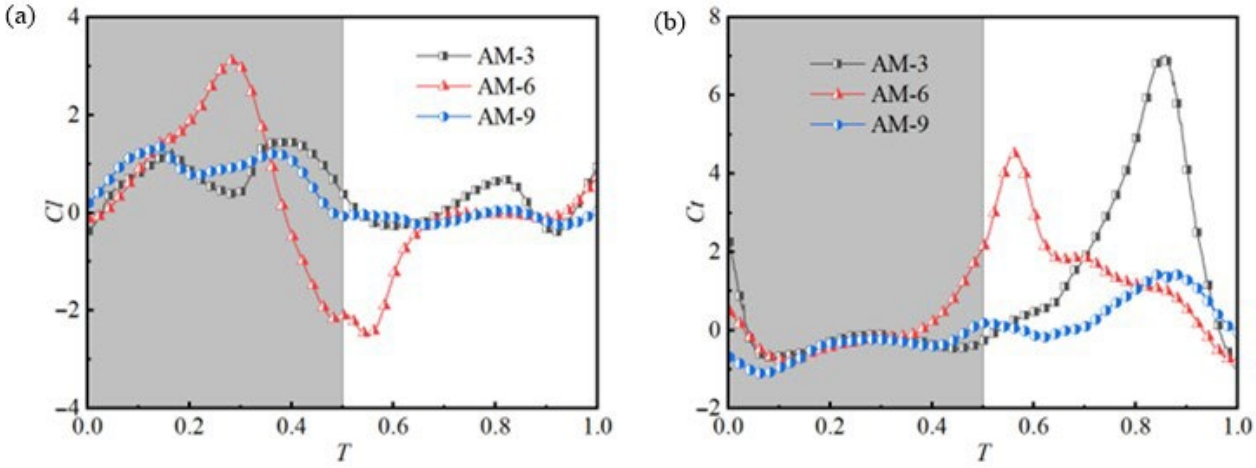

Figure 15. The time history of aerodynamic coefficients of AM-3, AM-6, and AM-9 in a short period: (**a**) lift coefficient; (**b**) propulsion coefficient.

As shown in Figure 15, the variation in lift is more pronounced for AM-3 compared to the other cases, with the highest peak observed. Additionally, the maximum lift generated by AM-3 in the aerodynamic force significantly exceeds that of the other cases. Consequently, the average propulsion performance of AM-3 is the highest among these cases.

To elucidate the variable mechanism responsible for instantaneous aerodynamic forces, the pressure contours corresponding to AM-3, AM-6, and AM-9 are provided in Figure 16a–d.

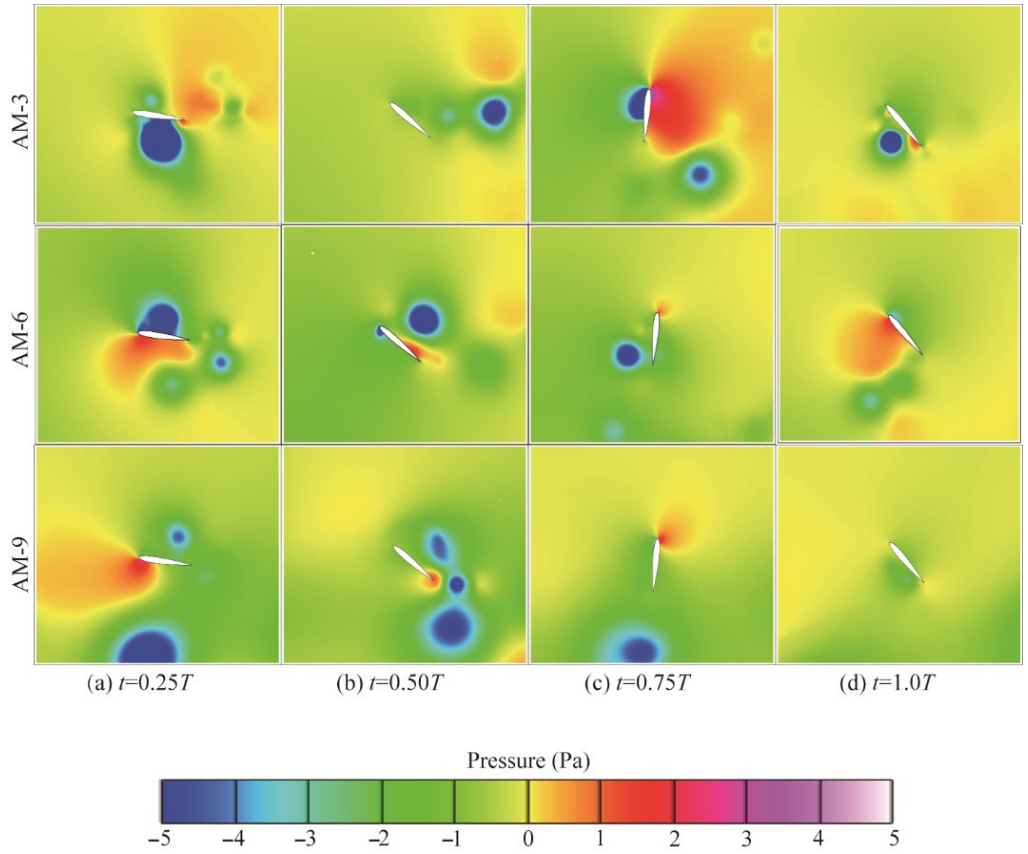

Figure 16. The pressure contours of AM-3, AM-6, and AM-9: (**a**) t = 0.25 T; (**b**) t = 0.50 T; (**c**) t = 0.75 T; (**d**) t = 1.0 T.

Figure 16a shows that pressure is applied to the lower surface in both the AM-6 and AM-9 cases, while the suction on the upper surface is stronger in the AM-6 case, resulting in a positive lift that is clearly greater than in the other cases. In Figure 16b, the suction on the upper surface transitions into pressure, leading to a reduction in lift that can even become negative—consistent with the trend shown in Figure 14a. Figure 16c illustrates how the pressure difference between the upper and lower surface is converted into propulsion; the pressure of the AM-3 case exceeds that of the others, producing the maximum propulsion at t = 0.75 T. In Figure 16d, the difference between suction and pressure is nearly balanced, allowing both lift and propulsion to return to their initial values.

An investigation into the mechanism by which plunge frequency acceleration affects the instantaneous aerodynamic force is conducted, with the corresponding vorticity contours of AM-3, AM-6, and AM-9 presented in Figure 17a,b.

Figure 17a shows that the LEV of AM-6 is attached to the upper surface. In contrast, the clockwise LEVs of AM-3 and AM-9 mode are shedding from the airfoil. This implies that the stall is delayed and the stall can alter the pressure distribution on the airfoil, thereby enhancing the lift in AM-6 at t = 0.25 T. In Figure 17b, the clockwise LEVs in all cases are continuously shed from the airfoil in the stall, indicating a likely reduction in lift. The shedding strength of AM-6 mode is the largest, implying that the reduction in AM-6 is the most significant at t = 0.50 T. This behavior aligns with the changes observed in the pressure contours in Figure 16b. As shown in Figure 17c, the TEVs for all configurations are expelled away from the airfoil, and their strength can be effectively increased, implying improved propulsion at t = 0.75 T. It is demonstrated that the anti-Kármán Vortex Street can enhance the propulsion of a flapping wing. In Figure 17d, the strength of the shedding TEVs decreases, suggesting that the propulsion returns to its baseline level.

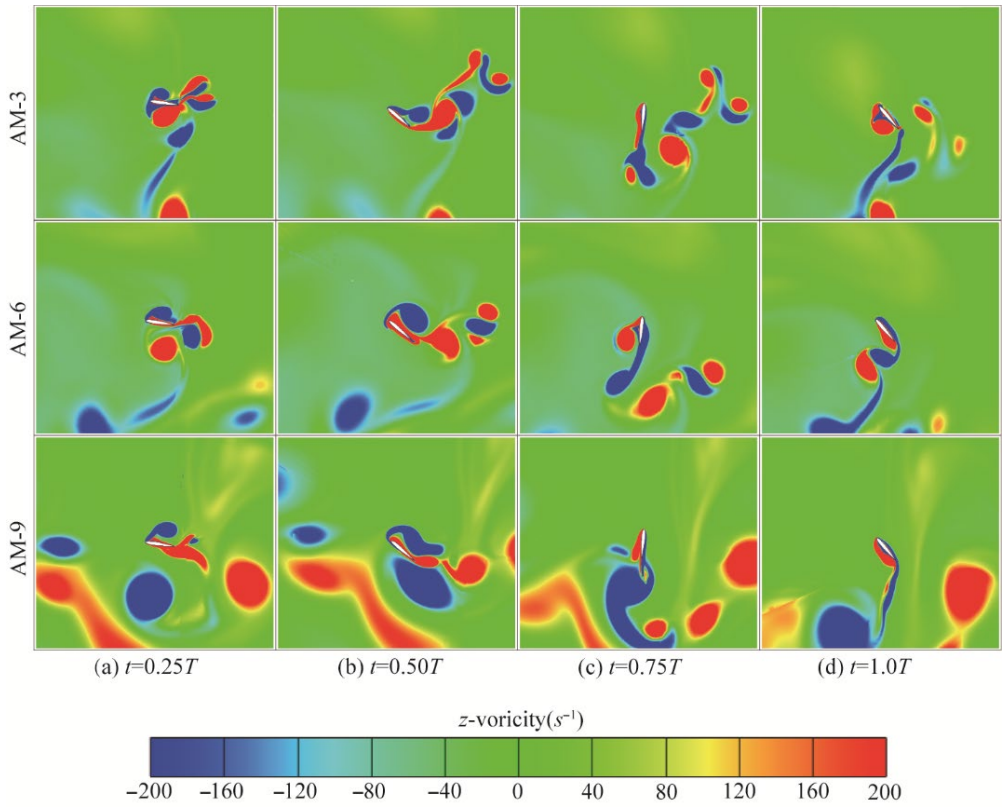

Figure 17. The vorticity contours of AM-3, AM-6, and AM-9: (**a**) t = 0.25 T; (**b**) t = 0.50 T; (**c**) t = 0.75 T; (**d**) t = 1.0 T.

4.2. Influence of Acceleration Coefficient on Aerodynamic Force

This subsection investigates the influence of acceleration coefficient n on aerodynamic performances by using CFD. The acceleration mode AM-3 is employed for the subsequent analysis. The acceleration coefficient n varies from 1.1 to 1.5 in steps of 0.1, and the corresponding average aerodynamic forces acting on the flapping wing at frequencies of 10 Hz, 20 Hz, and 30 Hz are presented in Figure 18.

As shown in Figure 18, the aerodynamic lift is enhanced by increasing the flapping frequency. Similarly, the hovering performance of a 2-DoF flapping wing improves with a higher acceleration coefficient, except for the average propulsion at the initial frequency of f = 10 Hz. The rate of increase in lift is slightly lower than that of propulsion. These results indicate that high acceleration combined with high frequency significantly improves the overall aerodynamic performance of the flapping wing.

The time history of aerodynamic forces at n = 1.1, 1.3, and 1.5 at the frequency of 20 Hz in a long period is depicted, as seen in Figure 19.

Figure 19 shows that the aerodynamic coefficients of the three cases are mostly greater than zero, with the minimum values across all cases being approximately similar. The peak values are observed at n = 1.5 and 1.1, corresponding to the highest and lowest values, respectively. It is found that increasing the acceleration coefficient n leads to an improvement in the average lift and propulsion.

The temporal progression of the aerodynamic force of the flapping wing in a short cycle is illustrated in Figure 20.

As demonstrated in Figure 20, the instantaneous lift and propulsion exhibit more pronounced fluctuations at n = 1.3 and 1.5 than at n = 1.1. Notably, the peak values for n = 1.3 and 1.5 are virtually identical. This observation explains why the average lift and propulsion are similar in these two cases but are markedly greater than those at n = 1.1.

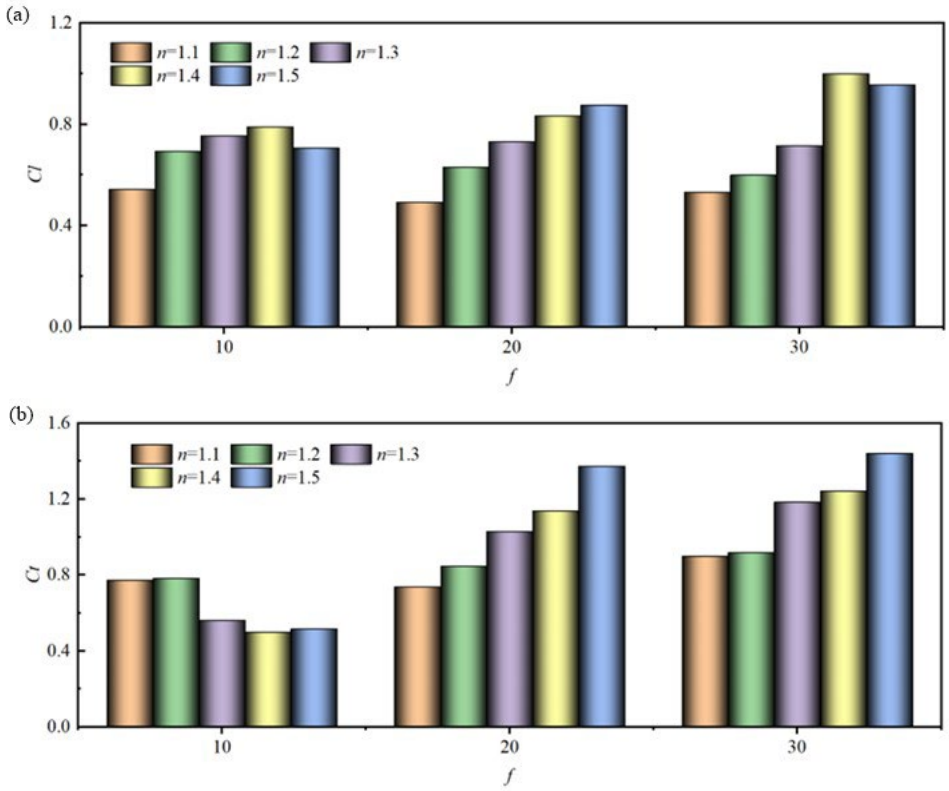

Figure 18. The average aerodynamic coefficient for different acceleration coefficients: (**a**) lift coefficient; (**b**) propulsion coefficient.

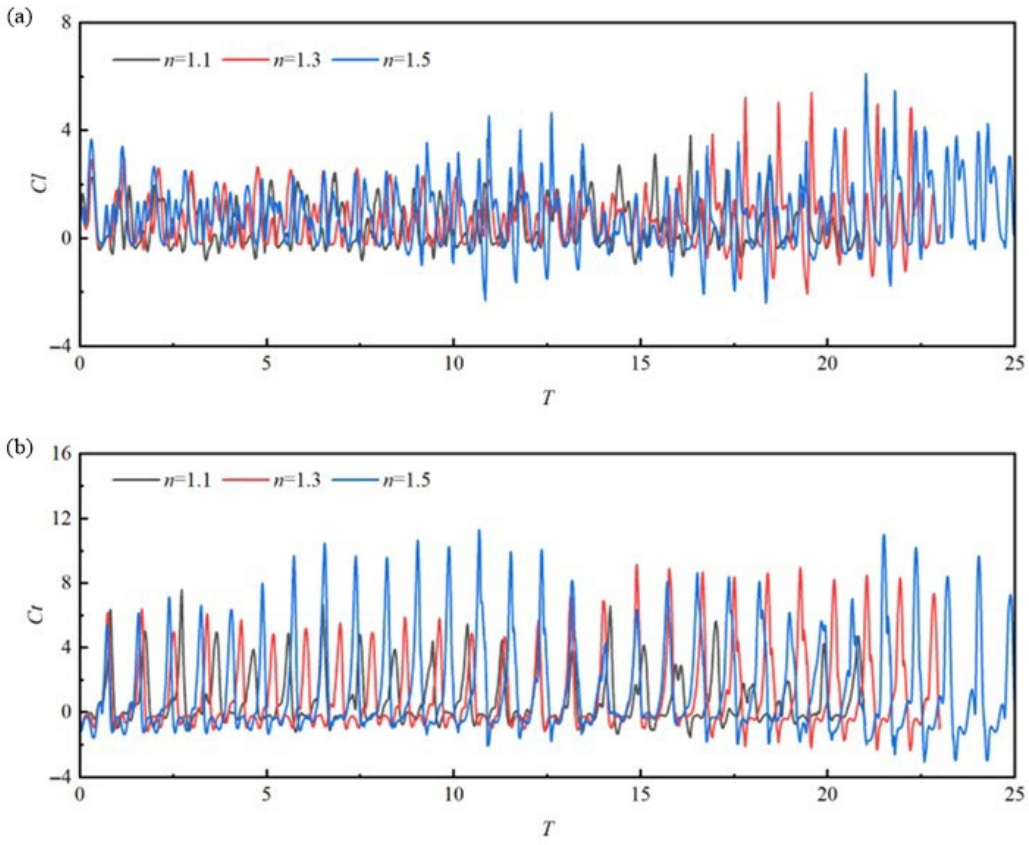

Figure 19. The time history of aerodynamic coefficients at n = 1.1, 1.3, and 1.5 in a long cycle: (**a**) lift coefficient; (**b**) propulsion coefficient.

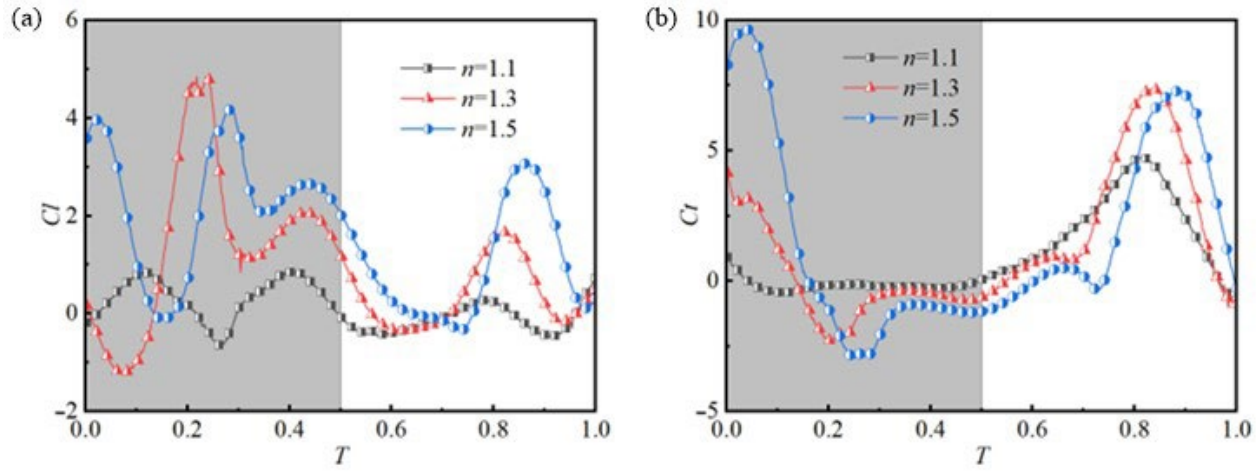

Figure 20. The time history of aerodynamic coefficients at n = 1.1, 1.3, and 1.5 in a short cycle: (**a**) lift coefficient; (**b**) propulsion coefficient.

To gain a deeper insight into the flow physics, the pressure contours at n = 1.1, 1.3, and 1.5 are shown in Figure 21a–d.

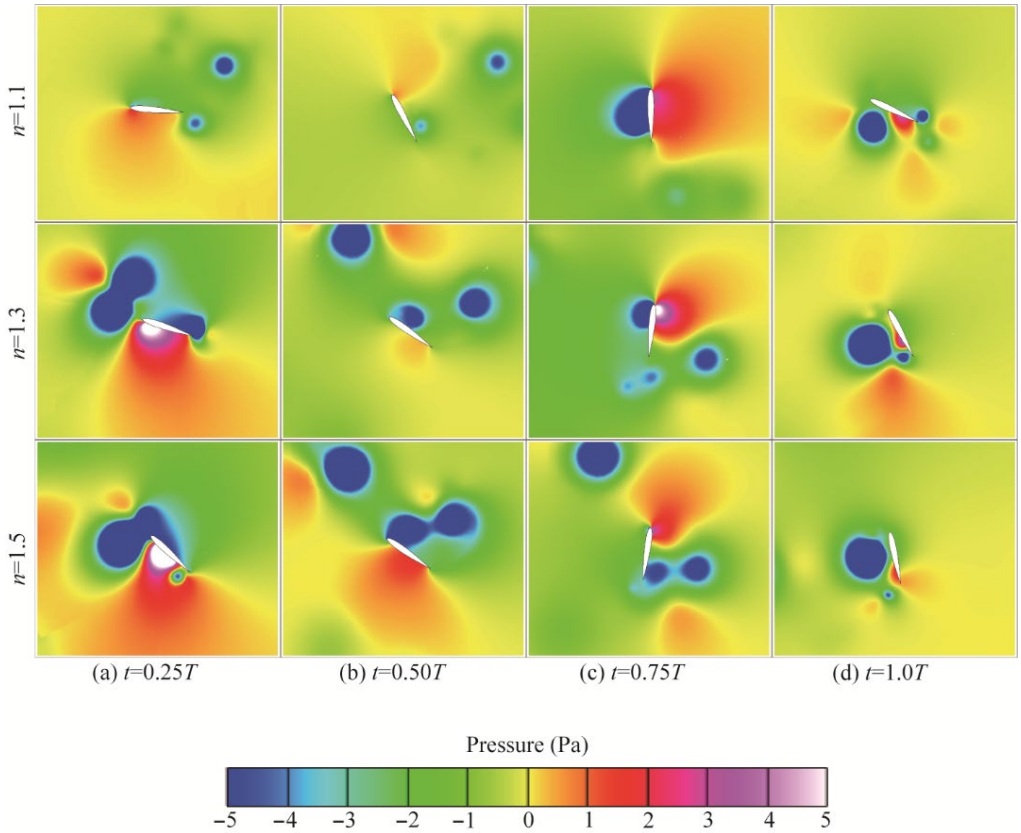

Figure 21. The pressure contours at n = 1.1, 1.3, and 1.5: (**a**) t = 0.25 T; (**b**) t = 0.50 T; (**c**) t = 0.75 T; (**d**) t = 1.0 T.

Figure 21a shows that under frequency acceleration, the angle of attack at n = 1.5 surpasses that of the other cases, leading to the maximum instantaneous lift observed at n = 1.5. In Figure 21b, the pressure on the lower surface decreases consistently across all cases, which causes a notable reduction in lift; it is noteworthy, however, that the lift at n = 1.5 remains the highest. As shown in Figure 21c, the pitching displacement approaches $\pi/2$ at the end of the upstroke, where pressure on the upper surface and suction on

the lower surface occur simultaneously, generating positive propulsion at t = 0.75 T. In Figure 21d, the suction and pressure on the surface are equalized, causing both lift and propulsion to approach zero.

To provide further insight into the changes in the pressure contours and instantaneous aerodynamic force, the corresponding vorticity contours at n = 1.1, 1.3, and 1.5 are shown in Figure 22a–d.

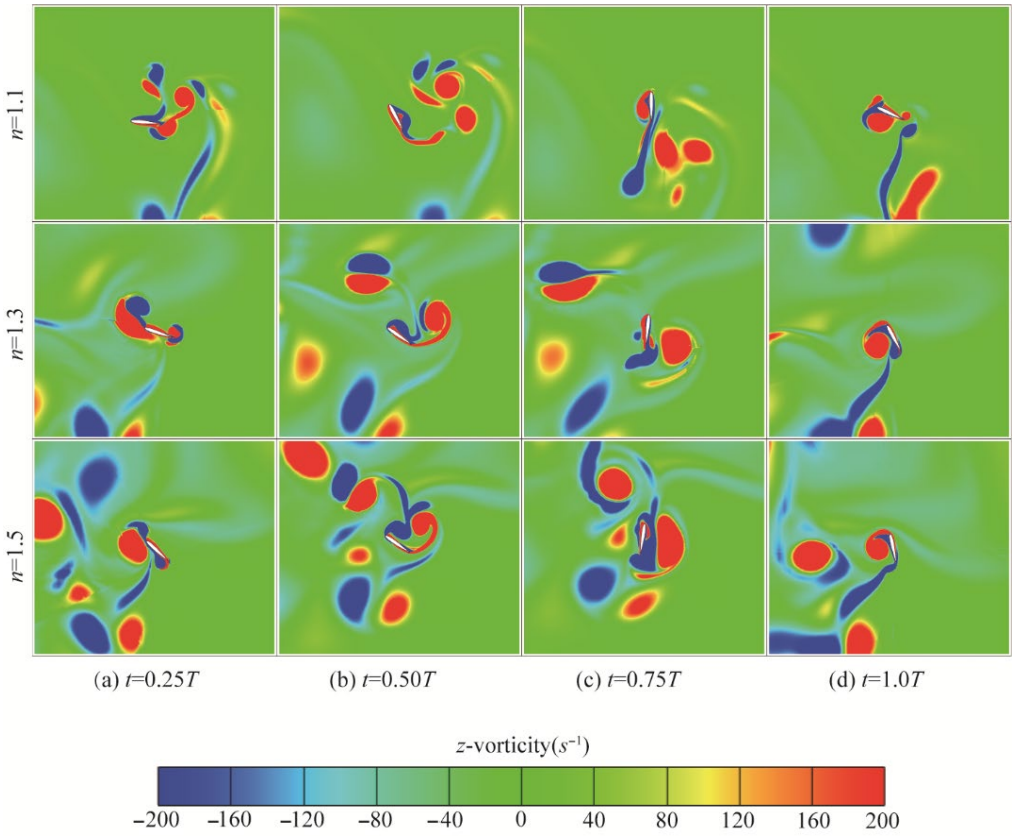

Figure 22. The vorticity contours at n = 1.1, 1.3, and 1.5: (**a**) t = 0.25 T; (**b**) t = 0.50 T; (**c**) t = 0.75 T; (**d**) t = 1.0 T.

As illustrated in Figure 22a, the LEVs at n = 1.1, 1.3, and 1.5 are consistently attached to the airfoil surface, and the angles of attack at n = 1.3 and 1.5 are significantly greater than that at n = 1.1. It is demonstrated that the LEV attachment can enhance the instantaneous lift, but the influence of the angle of attack is more pronounced, which explains the variation observed in Figure 21a. In Figure 22b, the attachment of clockwise LEVs in the stall leads to a reduction in lift. The angle of attack at n = 1.1 is more than that at other cases; therefore, the instantaneous lift at n = 1.1 is minimal. It is implied that the attachment of a clockwise LEV can weaken the suction, corresponding to the change in pressure contours in Figure 21b; the lift reduction is more pronounced by the stall. Figure 22c shows that both the strength and size of TEVs are enhanced, demonstrating that the propulsion is effectively increased at t = 0.75 T under the anti-Kármán Vortex Street. Meanwhile, Figure 22d illustrates that the strength of the shedding LEVs is diminished, resulting in a decrease in propulsion that eventually returns to its initial level.

5. Conclusions

This paper presents numerical simulations for solving the incompressible Navier–Stokes equations, with the aim of evaluating the aerodynamic performance of a 2-DoF flapping wing in hovering. The flapping motion under the FAE is accurately represented by a fitted

model derived from the wingtip trajectory over a cycle. By using CFD, the effect of frequency acceleration on aerodynamic performance has been investigated in plunging, pitching, and a combined pitching–plunging motion. The main findings are summarized as follows:

The acceleration mode exerted a marked influence on the aerodynamic performance of the 2-DoF flapping wing. Among the modes evaluated, AM-3 is identified as optimal, yielding a 1.2-fold enhancement in lift and a 2.1-fold improvement in propulsion compared to the case without acceleration. The introduction of acceleration during positive and negative pitching effectively enhances lift—shifting its value from negative to positive—while increasing propulsion by factors of 4.25 and 3.5, respectively, relative to the condition without pitching acceleration. This behavior shift is attributed to the delayed stall of the LEV and the shedding of the TEV. In plunge motion, the average lift is elevated to a positive value, with propulsion improved by factors of 2.4 and 1.85 under negative and positive acceleration, respectively. At a lower flapping frequency (f = 10 Hz), increasing the acceleration coefficient from 1.1 to 1.5 results in only marginal aerodynamic gains. In contrast, at a higher frequency (f = 30 Hz), the lift and propulsion are enhanced by factors of 1.83 and 1.6, respectively; however, the growth rate of aerodynamic forces diminished when the acceleration coefficient n exceeded 1.3. The evolution of the flow field, illustrated through pressure and vorticity contours, further elucidated the underlying mechanism associated with an increase in the acceleration coefficient.

In the future, numerical simulations will be performed using 3D models rather than the current 2D approach. Aerodynamic experiments will also be conducted to validate the accuracy of the numerical results. Furthermore, a flapping wing controller based on the frequency acceleration principle will be designed to further improve flight performance. Collectively, these findings provide valuable insights, offering potential strategies for optimizing the kinematic design of flapping wing drones.

Author Contributions: Conceptualization, F.K. and L.Q.; methodology, Z.L.; software, Z.L.; validation, F.K.; formal analysis, J.L.; investigation, J.L.; resources, F.K.; data curation, L.Q.; writing—original draft preparation, F.K.; writing—review and editing, F.K.; visualization, Z.L.; supervision, L.Q.; project administration, J.L.; funding acquisition, Z.L. All authors have read and agreed to the published version of the manuscript.

Funding: This research was funded by the Liaoning Provincial Science and Technology Joint Program (Natural Science Foundation—General Project), grant number 2025-MSLH-560.

Data Availability Statement: The data are contained within article.

Conflicts of Interest: The authors declare no conflicts of interest.

References

1. Chen, L.; Zhang, Y.; Zhou, C.; Wu, J. Aerodynamic mechanisms in bio-inspired micro air vehicles: A review in the light of novel compound layouts. *IET Cyber-Syst. Robot.* **2019**, *1*, 2–12. [CrossRef]
2. Salami, E.; Thomas, A.; Montazer, E.; Ghazali, N.N.N. A review of aerodynamic studies on dragonfly flight. *Proc. Inst. Mech. Eng. Part C J. Mech. Eng. Sci.* **2019**, *233*, 6519–6537. [CrossRef]
3. Hedrick, T.L.; Tobalske, B.W.; Ros, I.G.; Warrick, D.R.; Biewener, A.A. Morphological and kinematic basis of the hummingbird flight stroke: Scaling of flight muscle transmission ratio. *Proc. R. Soc. B Biol. Sci.* **2012**, *279*, 1986–1992. [CrossRef] [PubMed]
4. Schwegmann, A.; Lindemann, J.P.; Egelhaaf, M. Temporal statistics of natural image sequences generated by movements with insect flight characteristics. *PLoS ONE* **2014**, *9*, e110386. [CrossRef] [PubMed]
5. Han, J.H.; Han, Y.J.; Yang, H.H.; Lee, S.-G.; Lee, E.-H. A Review of Flapping Mechanisms for Avian-Inspired Flapping-Wing Air Vehicles. *Aerospace* **2023**, *10*, 554. [CrossRef]
6. Phillips, N. Experimental Unsteady Aerodynamics Relevant to Insect-Inspired Flapping-Wing Micro Air Vehicles. Master's Thesis, Cranfield University, Bedford, UK, 2011.
7. Han, C. Investigation of unsteady aerodynamic characteristics of a seagull wing in level flight. *J. Bionic Eng.* **2009**, *6*, 408–414. [CrossRef]

8. Dickinson, M.H.; Lehmann, F.O.; Sane, S.P. Wing rotation and the aerodynamic basis of insect flight. *Science* **1999**, *284*, 1954–1960. [CrossRef]
9. Tarascio, M.J.; Ramasamy, M.; Chopra, I.; Leishman, J.G. Flow visualization of micro air vehicle scaled insect-based flapping wings. *J. Aircr.* **2005**, *42*, 385–390. [CrossRef]
10. Wang, J.K.; Sun, M. A computational study of the aerodynamics and forewing-hindwing interaction of a model dragonfly in forward flight. *J. Exp. Biol.* **2005**, *208*, 3785–3804. [CrossRef]
11. Ansari, S.A.; Zbikowski, R.; Knowles, K. Non-linear unsteady aerodynamic model for insect-like flapping wings in the hover. Part 1: Methodology and analysis. *Proc. Inst. Mech. Eng. Part G J. Aerosp. Eng.* **2006**, *220*, 61–83. [CrossRef]
12. Nguyen, T.T.; Byun, D. Two-Dimensional aerodynamic models of insect flight for robotic flapping wing mechanisms of maximum efficiency. *J. Bionic Eng.* **2008**, *5*, 1–11. [CrossRef]
13. Orlowski, C.T.; Girard, A.R. Modeling and simulation of nonlinear dynamics of flapping wing micro air vehicles. *AIAA J.* **2011**, *49*, 969–981. [CrossRef]
14. Han, J.S. Interaction of the wakes of two flapping wings on control forces and moment. *Aerosp. Sci. Technol.* **2021**, *115*, 106794. [CrossRef]
15. Zhang, Y.; Wang, Z. An experimental study of the unsteady vortex structures of a clapping-wing micro air vehicle. *Int. J. Micro Air Veh.* **2022**, *14*, 17568293221125846. [CrossRef]
16. Martínez, G.B.; Van Oudheusden, B.W.; Sciacchitano, A.; Karásek, M. Large-scale volumetric flow visualization of the unsteady wake of a flapping-wing micro air vehicle. *Exp. Fluids* **2020**, *61*, 16. [CrossRef]
17. Aono, H.; Liu, H. Flapping wing aerodynamics of a numerical biological flyer model in hovering flight. *Comput. Fluids* **2013**, *85*, 85–92. [CrossRef]
18. Dahmani, F.; Sohn, C.H. Effects of advance ratio on elytra-hindwing interaction in forward flying Coleopteran beetle. *J. Mech. Sci. Technol.* **2018**, *32*, 5703–5710. [CrossRef]
19. Jones, M.; Yamaleev, N.K. Effect of lateral, downward, and frontal gusts on flapping wing performance. *Comput. Fluids* **2016**, *140*, 175–190. [CrossRef]
20. Fu, J.J.; Hefler, C.; Qiu, H.H.; Shyy, W. Effects of aspect ratio on flapping wing aerodynamics in animal flight. *Acta Mech. Sin.* **2014**, *30*, 776–786. [CrossRef]
21. Bhat, S.S.; Thompson, M.C. Effect of leading-edge curvature on the aerodynamics of insect wings. *Int. J. Heat Fluid Flow* **2022**, *93*, 108898. [CrossRef]
22. Au, L.T.K.; Phan, H.V.; Park, S.H.; Park, H.C. Effect of corrugation on the aerodynamic performance of three-dimensional flapping wings. *Aerosp. Sci. Technol.* **2020**, *105*, 106041. [CrossRef]
23. Bie, D.; Li, D. Numerical analysis of the wing–wake interaction of tandem flapping wings in forward flight. *Aerosp. Sci. Technol.* **2022**, *121*, 107389. [CrossRef]
24. Zhu, J.; Lei, B. Effect of wing-wing interaction on the propulsive performance of two flapping wings at biplane configuration. *Appl. Bionics Biomech.* **2018**, *2018*, 8901067. [CrossRef] [PubMed]
25. Li, L.; Xu, J.; Gao, Y.; Yang, J.; Bai, F.; Wang, Y. Unsteady aerodynamic characteristics of a bionic flapping wing in three-dimensional composite motion. *AIP Adv.* **2022**, *12*, 015109. [CrossRef]
26. Wu, T.; Song, B.F.S.; Song, W.P.; Yang, W.; Xue, D.; Han, Z. Lift performance enhancement for flapping airfoils by considering surging motion. *Chin. J. Aeronaut.* **2022**, *35*, 194–207. [CrossRef]
27. Mekadem, M.; Chettibi, T.; Oualli, H.; Hanchi, S. Thrust enhancement of a flapping airfoil using a non-sinusoidal motion trajectory. *J. Braz. Soc. Mech. Sci. Eng.* **2021**, *43*, 201–218. [CrossRef]
28. Lang, X.Y.; Song, B.F.; Yang, W.Q.; Song, W. Aerodynamic performance of owl-like airfoil undergoing bio-inspired flapping kinematics. *Chin. J. Aeronaut.* **2021**, *34*, 239–252. [CrossRef]
29. Boudis, A.; Bayeul-Laine, A.C.; Benzaoui, A.; Oualli, H.; Guerri, O.; Coutier-Delgosha, O. Numerical investigation of the effects of nonsinusoidal motion trajectory on the propulsion mechanisms of a flapping airfoil. *J. Fluids Eng.* **2019**, *141*, 041106. [CrossRef]
30. Wang, C.; Zhou, C.; Xie, P. Numerical investigation into the effects of stroke trajectory on the aerodynamic performance of insect hovering flight. *J. Mech. Sci. Technol.* **2016**, *30*, 1659–1669. [CrossRef]
31. Sarkar, S.; Chajjed, S.; Krishnan, A. Study of asymmetric hovering in flapping flight. *Eur. J. Mech.-B/Fluids* **2013**, *37*, 72–89. [CrossRef]
32. Younsi, A.; El-Hadj, A.A.; Abd Rahim, S.Z.; Rezoug, T. Effects of the wing spacing, phase difference, and downstroke ratio on flapping tandem wings. *Proc. Inst. Mech. Eng. Part C J. Mech. Eng. Sci.* **2022**, *236*, 4689–4712. [CrossRef]
33. Hu, F.; Wang, Y.; Li, D.; Liu, X. Effects of asymmetric stroke deviation on the aerodynamic performance of flapping wing. *Proc. Inst. Mech. Eng. Part G J. Aerosp. Eng.* **2023**, *237*, 480–499. [CrossRef]
34. Lang, X.; Song, B.; Yang, W.; Yang, X.; Xue, D. Sensitivity Analysis of Wing Geometric and Kinematic Parameters for the Aerodynamic Performance of Hovering Flapping Wing. *Aerospace* **2023**, *10*, 74. [CrossRef]

35. Li, H.; Nabawy, M.R.A. Effects of Stroke Amplitude and Wing Planform on the Aerodynamic Performance of Hovering Flapping Wings. *Aerospace* **2022**, *9*, 479. [CrossRef]
36. Zhu, J.Y.; Zhou, C.Y. Aerodynamic performance of a two-dimensional flapping wing in asymmetric stroke. *Proc. Inst. Mech. Eng. Part G J. Aerosp. Eng.* **2014**, *228*, 641–651. [CrossRef]
37. Wang, T.R.; Liu, N.; Yuan, L.; Wang, K.-X.; Sheng, X.-J. Iterative least square optimization for the weights of NURBS curve. *Math. Probl. Eng.* **2022**, *2022*, 5690564. [CrossRef]
38. Wang, Z.J. Two-dimensional mechanism for insect hovering. *Phys. Rev. Lett.* **2000**, *85*, 2216–2219. [CrossRef]

Disclaimer/Publisher's Note: The statements, opinions and data contained in all publications are solely those of the individual author(s) and contributor(s) and not of MDPI and/or the editor(s). MDPI and/or the editor(s) disclaim responsibility for any injury to people or property resulting from any ideas, methods, instructions or products referred to in the content.